

## **A participatory sensing approach to characterize ride quality**

Raj Bridgelall

North Dakota State University, Upper Great Plains Transportation Institute, P.O. Box 863676, Plano, TX 75086

### **ABSTRACT**

Rough roads increase vehicle operation and road maintenance costs. Consequently, transportation agencies spend a significant portion of their budgets on ride-quality characterization to forecast maintenance needs. The ubiquity of smartphones and social media, and the emergence of a connected vehicle environment present lucrative opportunities for cost-reduction and continuous, network-wide, ride-quality characterization. However, there is a lack of models to transform inertial and position information from voluminous data flows into indices that transportation agencies currently use. This work expands on theories of the Road Impact Factor introduced in previous research. The index characterizes road roughness by aggregating connected vehicle data and reporting roughness in direct proportion to the International Roughness Index. Their theoretical relationships are developed, and a case study is presented to compare the relative data quality from an inertial profiler and a regular passenger vehicle. Results demonstrate that the approach is a viable alternative to existing models that require substantially more resources and provide less network coverage. One significant benefit of the participatory sensing approach is that transportation agencies can monitor all network facilities continuously to locate distress symptoms, such as frost heaves, that appear and disappear between ride assessment cycles. Another benefit of the approach is continuous monitoring of all high-risk intersections such as rail grade crossings to better understand the relationship between ride-quality and traffic safety.

**Keywords:** Accelerometer, International Roughness Index, Road Impact Factor, pavement deterioration forecasting, connected vehicle initiative, time-wavelength-intensity-transform, quarter-car, impulse response, discrete Fourier transform, vehicle probe data.

### **1. INTRODUCTION**

The Connected Vehicle initiative of the United States Department of Transportation (USDOT) is one of their largest and most transformational research programs in Intelligent Transportation Systems. Vehicle manufacturers have teamed with the research community to produce technology that will help in the campaign towards zero highway deaths, as well as a several-fold capacity enhancement of the existing physical network by enabling ubiquitous vehicle communications<sup>1</sup>. A majority of the connected-vehicle-related research focuses on ways to enhance safety and mobility. However, relatively few studies examine performance measures to optimize asset management such as predictive pavement maintenance. This research links the International Roughness Index (IRI) to statistics of road roughness derived from the aggregate inertial responses of connected vehicles.

Several studies found a correlation between the vertical acceleration of vehicles and the International Roughness Index (IRI). Those characterizations are based on heuristics<sup>2</sup> or use machine learning techniques<sup>3</sup> such as neural networks to calibrate empirical models with responses from individual vehicles. This study establishes a theoretical foundation to derive a proportionality relationship from basic principles that relate the average vertical acceleration of vehicles traveling a segment to the IRI.

This paper is organized as follows: Section 2 reviews the classic derivation of a quarter-car response and relates it to the IRI model using a standard set of suspension parameters defined as the Golden Car. A review of the Road Impact Factor (RIF) derived in previous works by the author is also presented to highlight its relationship with the quarter-car response. Section 3 introduces a methodology for deriving their proportionality constants based on the principles of linear time-invariant systems (LTI) and their impulse responses. The wavelength sensitivities of each model is presented and a wavelength unbiased model based on the RIF is introduced. Section 4 describes the data collection equipment, test site, data format, and data processing used to validate the models. Section 5 presents the results of a case study to characterize

the relative RIF distribution and their chi-squared statistics for road segments of a known roughness levels. This section also demonstrates a multi-resolution distress symptom localization capability of the RIF and an example of IRI estimation from RIF measurements. The final section summarizes and concludes the study.

## 2. MODEL REVIEW

The following sections review the quarter-car, IRI, and RIF models to highlight their mathematical relationships and dependencies on common parameters of a damped mass-spring system.

### 2.1 Vehicle suspension response model

From Newton's law, the resultant vertical force  $F_z$  acting on the sprung mass  $m_s$  of a damped mass-spring system is  $F_z = m_s \ddot{z}$ . The upward vertical acceleration is  $\ddot{z}(t)$ . The components of the vertical force are the downward acceleration  $-m_s g$  due to gravity  $g$ , the upward resistance to vertical velocity  $\dot{z}(t)$  with viscous damping coefficient  $c_s$ , and the upward spring force  $k_s(h-z)$  with spring stiffness  $k_s$  and compression distance  $h$ . Rolling across the longitudinal profile creates an upward forcing function  $f_z(t)$  on the tire. The sum of these forces yields the motion equation for a damped mass-spring model

$$m_s \ddot{z}(t) = -m_s g - c_s \dot{z}(t) + k_s [h - z(t)] + f_z(t) \quad (1)$$

When the system is at rest at time  $t = 0$  the vertical reference plane is at  $z(0) = 0$ . Hence the equilibrium condition is

$$-m_s g + k_s h = 0 \quad (2)$$

Substituting equation (2) into equation (1) yields the second order, non-homogeneous linear differential equation of motion for the sprung mass response to the forcing function

$$\ddot{z}(t) + \frac{c_s}{m_s} \dot{z}(t) + \frac{k_s}{m_s} z(t) = \frac{1}{m_s} f_z(t) \quad (3)$$

The natural frequency of the sprung mass system,  $\omega_s$ , is defined as

$$\omega_s = \sqrt{\frac{k_s}{m_s}} \quad (4)$$

The damping ratio,  $\zeta_s$ , is defined as

$$\zeta_s = \frac{1}{2\omega_s} \frac{c_s}{m_s} = \frac{c_s}{2\sqrt{k_s m_s}} \quad (5)$$

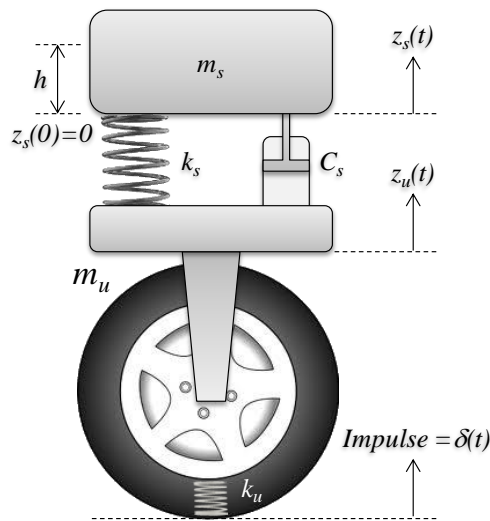


Figure 1. Damped mass-spring model of a quarter-car.

This expression yields a normalized model where the mass-spring system dynamics is completely described by its natural frequency and damping ratio

$$\ddot{z}(t) + 2\zeta_s \omega_s \dot{z}(t) + \omega_s^2 z(t) = \delta(t) \tag{6}$$

where  $f_z(t)/m_s$  is replaced by an impulse excitation  $\delta(t)$  to determine the impulse response. The standard quarter-car model consists of a series combination of mass-spring systems as shown in Figure 1. The sprung mass represents one-quarter of the vehicle mass riding on a spring suspension system. Studies in vehicle dynamics refer to the tire and associated components below the suspended body as the unsprung mass and above it as the sprung mass.

**2.2 The IRI model**

The IRI is defined as the accumulated, absolute rate difference between the sprung and unsprung mass motion of a special quarter-car such that

$$IRI = \frac{1}{L} \int_0^{L/\bar{\sigma}} |\dot{z}_s(t) - \dot{z}_u(t)| dt \tag{7}$$

The longitudinal distance traveled is  $L$  and the constant speed  $\bar{\sigma}$  is 80 km/h. The first derivatives of the sprung and unsprung mass vertical motions are  $\dot{z}_s(t)$  and  $\dot{z}_u(t)$  respectively. An international committee defined the special quarter-car parameters and referred to it as the Golden Car<sup>4</sup>. Table 1 summarizes those parameters, normalized to the sprung mass.

Table 1. Golden Car model parameters.

Parameter	Value	Unit
$k_s/m_s$	63.3	$s^{-2}$
$k_u/m_s$	653	$s^{-2}$
$c_s/m_s$	6.0	$s^{-1}$
$m_u/m_s$	0.15	-

The unsprung mass and its associated spring stiffness are  $m_u$  and  $k_u$  respectively. Some researchers point out that others often ignore the damping coefficient  $c_u$  of the unsprung mass model but a reasonable estimate would be about 15% of the sprung mass damping coefficient<sup>5</sup>. Applying these values to Equations (4) and (5) yield the Golden Car resonant frequencies and damping ratios summarized in Table 2.

Table 2. Damped mass-spring parameters for the Golden Car.

Parameter	Units	Sprung Mass	Unsprung Mass
Resonant Frequency (f)	Hz	1.27	10.50
Damping Ratio ( $\zeta$ )	-	0.38	0.05

Transportation agencies use a software program to produce the vertical forcing function numerically by first computing the vertical acceleration that results from traversing a longitudinal profile at 80 km/h. The program then uses Equation (3) to determine the Golden Car suspension response needed to evaluate the IRI using Equation (7).

**2.3 The RIF model**

The second derivative of the sprung mass response,  $\ddot{z}(t)$  is directly proportional to the vertical acceleration sensed by an accelerometer in the vehicle. The signal produced is  $g_z = \gamma_z \ddot{z}(t)$  where  $\gamma_z$  is a sensor constant. As defined in the author’s previous research<sup>6</sup>, the RIF per unit length  $L$  of road segment traversed at instantaneous speed  $\sigma(t)$  and average speed  $\bar{\sigma}$  is

$$R_{\bar{\sigma}}^L = \gamma_z \sqrt{\frac{1}{L} \int_0^{L/\bar{\sigma}} |\ddot{z}(t)\sigma(t)|^2 dt} \tag{8}$$

The RIF is effectively the square root of the vertical acceleration energy per unit distance. Although a RIF unit is in  $m^{1/2} \cdot s^{-1}$  it is practically interpreted as the average g-force experienced per meter of longitudinal travel.

### 3. METHODOLOGY

The RIF and IRI are both linear time-invariant transformations (LTI) of the sprung and unsprung mass motions; therefore, they must be directly proportional. To derive a constant of direct proportionality, this section finds their impulse responses and computes the ratio of their respective indices.

#### 3.1 Convergence of the IRI impulse response

Solving Equation (6) for the under-damped case where  $0 < \zeta < 1$  yields

$$z_{\delta}(t) = u(t) \frac{1}{\omega_0 \sqrt{1-\zeta^2}} \exp(-\zeta\omega_0 t) \sin(\omega_0 t \sqrt{1-\zeta^2}) \quad (9)$$

where  $z_{\delta}(t)$  is the impulse response and  $u(t)$  is the Heaviside step function. The Golden Car response to an impulse excitation is the convolution of the sprung and unsprung mass impulse responses

$$z_{\delta G}(t) = z_{\delta s}(t) * z_{\delta u}(t) = \int_{-\infty}^{\infty} z_{\delta s}(\tau) z_{\delta u}(t-\tau) d\tau \quad (10)$$

where  $*$  is the convolution operator and  $z_{\delta s}(t)$  and  $z_{\delta u}(t)$  are the impulse responses of the quarter-car sprung and unsprung mass respectively. The accumulated absolute rate differences between the Golden Car impulse response and that of the unsprung mass is denoted  $IRI_{\sigma}^L$  where

$$IRI_{\sigma}^L = \int_0^{L/\sigma} |\dot{z}_{\delta G}(t) - \dot{z}_{\delta u}(t)| dt \quad (11)$$

The absolute value in Equation (11) hinders a closed form solution. Therefore, by numerical integration using the Golden Car parameters listed in Table 2, the functions  $z_{\delta G}(t)$  and  $IRI_{\sigma}^L(t)$  are as shown in Figure 2.

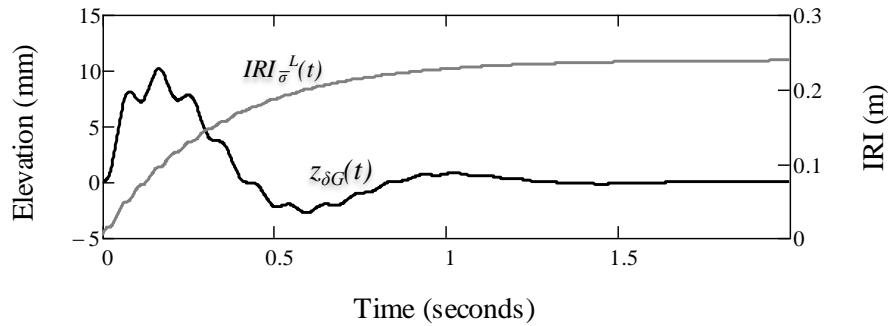


Figure 2. Impulse response of the Golden Car model and the resulting IRI.

The value at 2.0 seconds or equivalently at 44.5 meters is already within 0.2% of the value at one kilometer. That is, the practical IRI limit of integration for an impulse response is  $t = L/\sigma = 1000 \text{ meters}/80 \text{ km}\cdot\text{h}^{-1} = 45 \text{ seconds}$ . As observed through series expansion the value asymptotically approaches

$$\lim_{(L/\sigma) \rightarrow \infty} IRI_{\sigma}^L \cong \frac{1}{2} \left( \frac{1}{\omega_{Gs} \zeta_{Gs}} + \frac{1}{\omega_{Gu} \zeta_{Gu}} \right)^2 \frac{1}{\sqrt{(1-\zeta_{Gs}^2)(1-\zeta_{Gu}^2)}} \quad (12)$$

The parameters  $\omega_{Gs}$  and  $\omega_{Gu}$  denotes the Golden Car sprung and unsprung mass resonant frequencies in radians per second. Their corresponding damping ratios are denoted  $\zeta_{Gs}$  and  $\zeta_{Gu}$ .

#### 3.2 The RIF of the impulse response

The RIF converges to a proportion of the accelerometer signal energy  $E_{gz}$  such that

$$R_{\bar{\sigma}}^L = \gamma_z \bar{\sigma} \sqrt{\frac{1}{L} \int_0^{L/\bar{\sigma}} |g_z(t)|^2 dt} = \gamma_z \bar{\sigma} \sqrt{\frac{1}{L} \lim_{\varepsilon \rightarrow 0} \int_0^{T_\varepsilon} |g_z(t)|^2 dt} = \gamma_z \bar{\sigma} \sqrt{\frac{1}{L} E_{g_z}} \quad (13)$$

where  $T_\varepsilon = |g_z^{-1}(\varepsilon)|$  is the limit of integration when the vertical acceleration of the impulse response magnitude is negligibly small. The closed form expression for  $E_{g_z}$  in the limit as  $t$  approaches infinity is found by utilizing the distributive property of a LTI function to decompose the resultant vertical acceleration into a linear combination of the vertical accelerations from the individual damped mass-spring impulse responses such that

$$g_z(t) = \frac{d^2}{dt^2} [z_{\delta s}(t) * z_{\delta u}(t)] = \gamma_z [g_{\delta s}(t) + \rho_g g_{\delta u}(t)] \quad (14)$$

where  $g_z(t)$  is the resultant vertical acceleration;  $g_{\delta s}(t)$  and  $g_{\delta u}(t)$  are the vertical accelerations of the quarter-car sprung and unsprung mass impulse responses respectively. The parameter  $\rho_g$  is an estimate of the ratio between the sprung and unsprung mass acceleration magnitude components. The acceleration signal energy is calculated as

$$E_{g_z} \cong E_{\delta u} = \int_0^\infty [\gamma_z g_{\delta s}(t)]^2 dt + \int_0^\infty [\gamma_z \rho_g g_{\delta u}(t)]^2 dt = \gamma_z^2 \omega_{s\mu} \left( \zeta_{s\mu} + \frac{1}{4\zeta_{s\mu}} \right) + \gamma_z^2 \rho_g^2 \omega_{u\mu} \left( \zeta_{u\mu} + \frac{1}{4\zeta_{u\mu}} \right) \quad (15)$$

The parameters  $\omega_{s\mu}$  and  $\omega_{u\mu}$  denotes the average quarter-car sprung and unsprung mass resonant frequencies in radians per second. Their corresponding average damping ratios are denoted  $\zeta_{s\mu}$  and  $\zeta_{u\mu}$ . For the average suspension parameter<sup>7</sup>, the limit of integration,  $T_\varepsilon$  evaluates to about two seconds. Hence, the signal energy  $E_{g_z}$  is practically identical to the impulse response energy  $E_{\delta u}$ . Substituting the total energy from Equation (15) into the RIF model of Equation (13) and dividing by the converged IRI impulse response of Equation (12) provides a proportionality constant  $\kappa_{RI}$  between the RIF and IRI as

$$\kappa_{RI} = \frac{\bar{\sigma} \sqrt{\frac{1}{L} \gamma_z \sqrt{\omega_{s\mu} \left( \zeta_{s\mu} + \frac{1}{4\zeta_{s\mu}} \right) + \rho_g^2 \omega_{u\mu} \left( \zeta_{u\mu} + \frac{1}{4\zeta_{u\mu}} \right)}}}{\frac{1}{2} \left( \frac{1}{\omega_{Gs} \zeta_{Gs}} + \frac{1}{\omega_{Gu} \zeta_{Gu}} \right)^2 \frac{1}{\sqrt{(1-\zeta_{Gs}^2)(1-\zeta_{Gu}^2)}}} \quad (16)$$

Hence, the average proportionality constant for quarter-car impulse responses is a function of the mean suspension parameters and average speed of vehicles traversing a road segment.

### 3.3 Wavelength sensitivity

Traversing a road segment at a constant speed converts its spatial wavelengths in cycles per meter to temporal wavelengths in cycles per second. A damped mass-spring system is a mechanical filter that suppresses responses to wavelengths that are outside of its frequency response range. The quarter-car produces its maximum response to wavelengths that range from  $\bar{\sigma}/f_s$  to  $\bar{\sigma}/f_u$  meters where  $f_s$  and  $f_u$  are the sprung and unsprung mass resonance frequencies in units of hertz or equivalently cycles per second respectively. Hence the IRI response will dampen when the spatial frequency is lower than 17.6 meters-cycle<sup>-1</sup> and higher than 2.1 meters-cycle<sup>-1</sup> as shown in Figure 3.

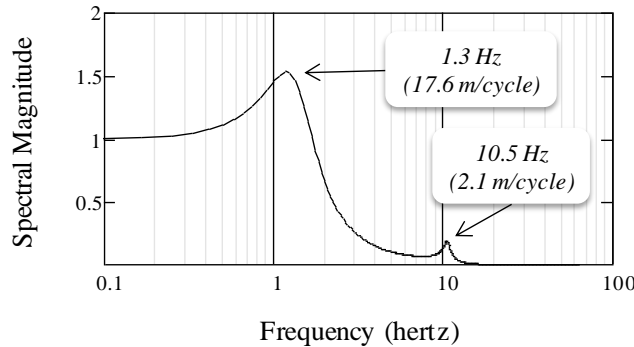


Figure 3. Spectral magnitude of the Golden Car impulse response.

The Golden Car frequency response is the Fourier transform of the impulse response defined in Equation (10). The result is mathematically equivalent to computing the Fourier transforms of the sprung and unsprung mass impulse responses, denoted  $\mathcal{F}\{z_{\delta s}(t)\} = Z_{\delta s}(\omega)$  and  $\mathcal{F}\{z_{\delta u}(t)\} = Z_{\delta u}(\omega)$  respectively, and then computing their product  $Z_{\delta s}(\omega) \cdot Z_{\delta u}(\omega)$ . The individual transforms are second-order low-pass filters  $Z_{\delta}(\omega)$  of the form

$$Z_{\delta}(\omega) = \frac{1}{\sqrt{1-\zeta^2}} \frac{1}{\omega^2 + (\zeta\omega + j\omega)^2} \quad (17)$$

Traveling the same profile at higher speeds will shift longer spatial wavelengths into the quarter-car frequency response band and shorter ones outside of it. Hence, the IRI can be insensitive to roughness from small cracks on a flat profile and yet be more sensitive to the spatial undulations of a hilly road with an otherwise smooth surface.

To remove such wavelength bias from the RIF, the author introduced the time-wavelength-intensity-transform (TWIT)<sup>6</sup> in previous work. It is a linear combination of the average RIF from traversals of different speed bands where the coefficients are the percentages of vehicles traveling in each band. The TWIT for a road segment  $k$  during an arbitrary time-interval  $\Delta P$  of time-index  $j$  is denoted  $\Psi_k[\Delta P_j]$  where

$$\Psi_k(\Delta P_j) = \frac{\sum_{w=1}^{B_k} \bar{R}_{\Delta\sigma_w}^{\Delta P_j}[k] \times N_{\Delta\sigma_w}^{\Delta P_j}[k]}{\sum_{w=1}^{B_k} N_{\Delta\sigma_w}^{\Delta P_j}[k]} \quad (18)$$

The speed-band or window size is  $\Delta\sigma$  and the window index is  $w$ . The average RIF of vehicles traversing segment  $k$ , within a speed band  $\Delta\sigma_w$ , and during time increment  $\Delta P_j$  is denoted as  $\bar{R}_{\Delta\sigma_w}^{\Delta P_j}[k]$ . The corresponding traversal volume is denoted as  $N_{\Delta\sigma_w}^{\Delta P_j}[k]$ . The total number of speed bands available for segment  $k$  is  $B_k$ . A key property of the TWIT is that it emphasizes roughness from longitudinal profile wavelengths that the vehicle population experiences at the most common speed ranges.

#### 4. DATA

The average IRI and RIF computed from data simultaneously collected with a laser-based inertial profiler provides experimental validation of their direct proportionality.

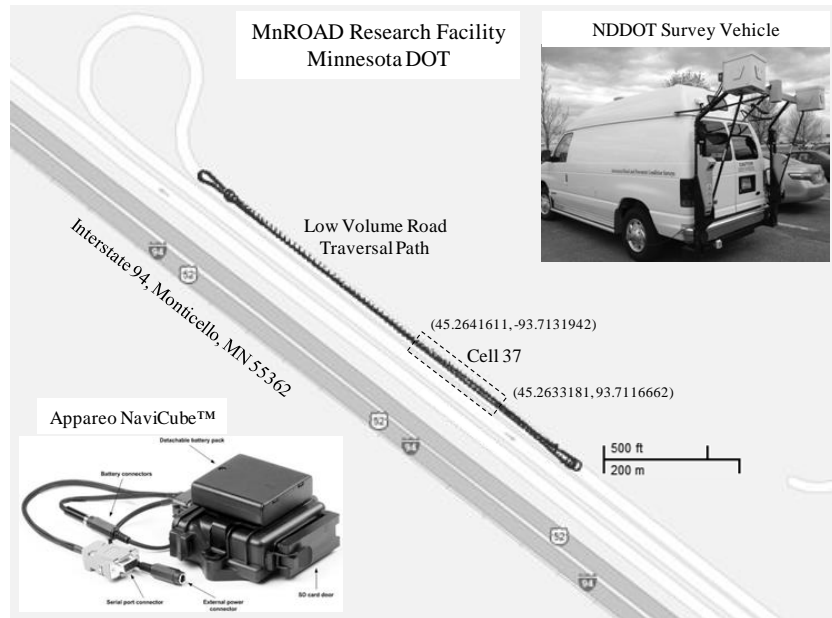


Figure 4. IRI and RIF traversal path and equipment at the MnROAD facilities.

A regular passenger vehicle is also used to compare RIF statistics for a road containing distinctly smooth and rough segments as well as a rail grade crossing. The data quality is assessed relative to their chi-squared fit with classic statistical distributions. The multi-resolution localization capability of the RIF is also demonstrated by identifying the location and roughness density of the rail-grade crossing at different spatial resolutions.

#### 4.1 Equipment and test site

A ruggedized GPS-accelerometer data logger, the NaviCube™ from Appareo Systems, was secured to the floor mat of a North Dakota Department of Transportation (NDDOT) Survey Vehicle. The data logger, shown in the bottom inset of Figure 4 sampled the vertical acceleration at approximately 125 hertz and updated the GPS coordinates at approximately 2 hertz. The NDDOT Survey Vehicle is a modified model E350 Ford van. It carries laser-based inertial profiling equipment that measures the profile elevation at approximately 3.8 centimeter intervals as the vehicle moves at a fixed speed. The equipment collected simultaneously the elevation profile and RIF data from six traversals of Cell 37, a 500 feet segment of the Minnesota Department of Transportation’s MnROAD research facility shown in Figure 4. Only six MnROAD traversals were afforded as part of the standard Inertial Profiler calibration procedure. However, the measurement variance was relatively low because the Inertial Profiler maintained a near constant speed and approximately the same wheel path for each traversal. The ratio of its ground speed standard deviation and the mean speed was much less than 0.1%. The consistency of those measurements served as a baseline for comparison with the data quality obtained from a regular passenger vehicle equipped with a consumer grade data logger.

To obtain the passenger vehicle vertical acceleration, an Apple iTouch with a data logger application (app) was placed flat on the dashboard of a 2007 Subaru Legacy sedan and driven 30 times along the selected road segment, Bolley Drive. Located on the North Dakota State University campus, this road segment contains a rail grade crossing that produces a noticeably rougher ride than the rest of the segment.

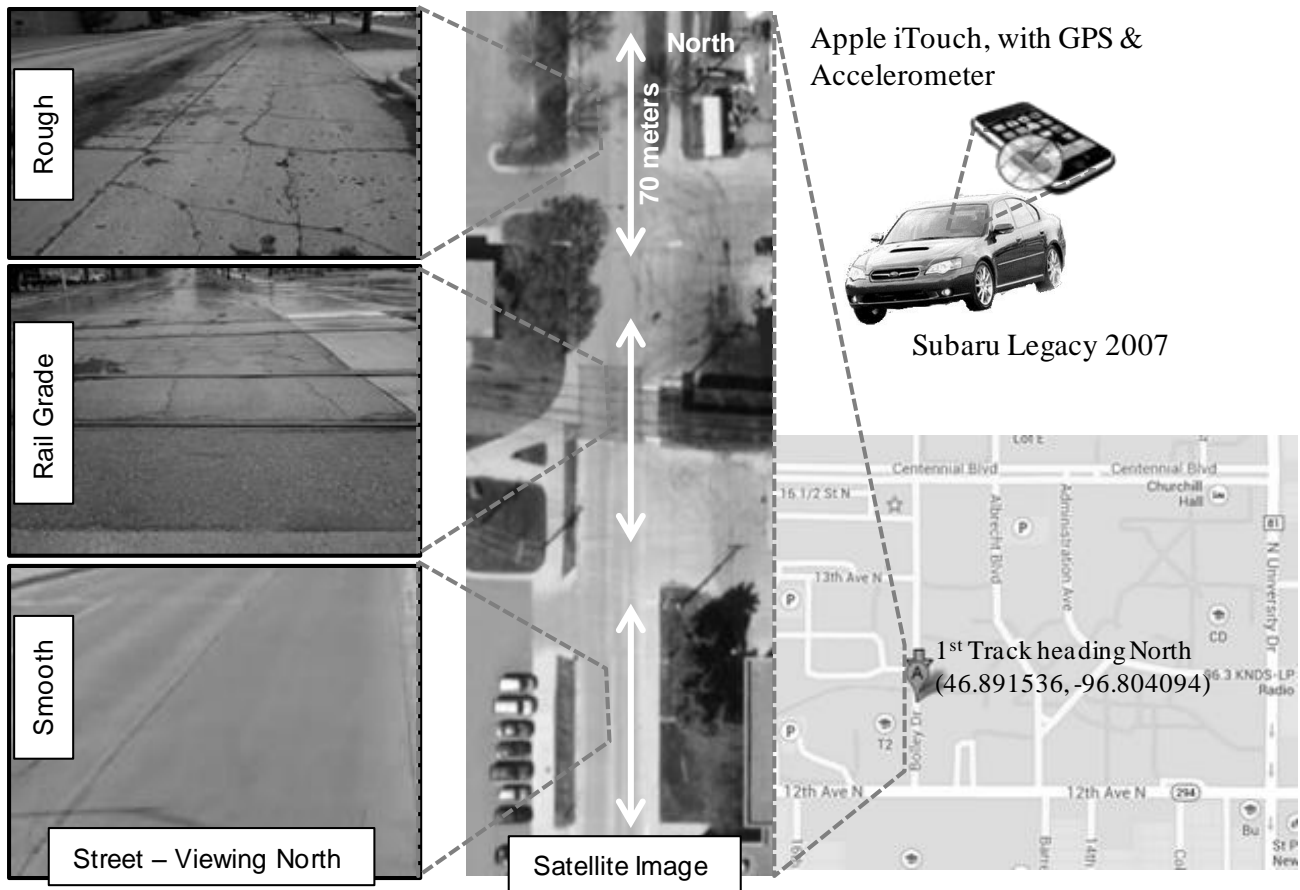


Figure 5. On street and satellite views of Bolley Drive sections analyzed, the passenger vehicle, and the data logger.

The crossing consists of four rails. The latitude and longitude of the first track crossed when heading north is as indicated in Figure 5. The 70 meter segment south of the crossing looks and feels significantly smoother than the 70 meter segment north of the crossing, but not as smooth as the MnROAD test path. Similarly, the north segment looks and feels much smoother than the 70 meter segment containing the crossing. The iTouch's GPS and accelerometer update rates were 1 and 64 hertz respectively. These rates are about half that of the NaviCube used to sample data from the MnROAD traversals.

## 4.2 Data format

The Inertial Profiler produced elevation profile samples in the \*.erd standard file format specified by the University of Michigan Transportation Research Institute (UMTRI). The Profile Viewing and Analysis (ProVAL) software from The Transtec Group then converted that data to an IRI value. As a standard format does not yet exist for RIF data, a comma separated value (CSV) file format shown Table 3 was used. The first row contains a header with labels for each column of data sampled from the sensors.

Table 3. Standard data format used to compute the RIF.

Time	Gz	Lat	Lon	Gspeed	Pitch	Roll	Yaw	Gx	Gy
114421	-1.0165	45.27234	-93.6994	16.92	-0.09375	2.375	-0.0625	-0.327	-0.0335
114429	-1.0185	45.27234	-93.6994	16.92	-0.625	1.6875	1.1875	-0.334	-0.041
114437	-1.027	45.27234	-93.6994	16.92	-0.90625	1.78125	-0.40625	-0.3315	-0.0405
114445	-1.0045	45.27234	-93.6994	16.92	0.90625	1.40625	0.28125	-0.3275	-0.0405
114453	-0.9845	45.27234	-93.6994	16.92	-0.25	1.375	-0.75	-0.324	-0.0425
114460	-0.9805	45.27234	-93.6994	16.92	0.1875	0.96875	0.0625	-0.3225	-0.05
114468	-1.005	45.27234	-93.6994	16.92	-0.125	1	0.3125	-0.335	-0.0555

The data columns are the sample period or "Time" is in milliseconds; "Lat" and "Lon" for latitude and longitude respectively in decimal format; "Gspeed" for the vehicle ground speed in  $m \cdot s^{-1}$ ; "Gz", "Gx", and "Gy" for the g-forces sensed in the vertical, lateral, and longitudinal directions respectively and normalized to  $9.81 m \cdot s^{-2}$ ; "Pitch," "Roll," and "Yaw" are the sensor orientation angles in degrees respectively.

## 4.3 Sensor orientation calibration

The resultant vertical acceleration in any sensor orientation is determined by multiplying the linear acceleration from each sensor axis by the magnitude of the vertical component of their rotated unit vector in the Cartesian plane. The amount of unit vector rotation  $\Pi_{xyz}$  is

$$\Pi_{xyz}(u_{xyz}, \psi, \theta, \phi) = \begin{bmatrix} 1 & 0 & 0 \\ 0 & \cos(\psi) & \sin(\psi) \\ 0 & -\sin(\psi) & \cos(\psi) \end{bmatrix} \begin{bmatrix} \cos(\theta) & 0 & -\sin(\theta) \\ 0 & 1 & 0 \\ \sin(\theta) & 0 & \cos(\theta) \end{bmatrix} \begin{bmatrix} \cos(\phi) & \sin(\phi) & 0 \\ -\sin(\phi) & \cos(\phi) & 0 \\ 0 & 0 & 1 \end{bmatrix} u_{xyz} \quad (19)$$

where  $\psi$ ,  $\theta$ , and  $\phi$  are the pitch, roll, and yaw angles produced by the gyroscope integrated in the smartphone. The unit vector  $u_{xyz} = [1 \ 1 \ 1]^T$  represents the composite of the lateral, longitudinal, and vertical directions respectively. The notation  $T$  represents the vector transpose matrix operator. Therefore, the resultant vertical acceleration  $G_z$  as a function of the sensor orientation is

$$G_z(\psi, \theta, \phi) = \sqrt{[G_{xu} \cdot \Pi_{xyz}(u_x, \psi, \theta, \phi)_z]^2 + [G_{yu} \cdot \Pi_{xyz}(u_y, \psi, \theta, \phi)_z]^2 + [G_{zu} \cdot \Pi_{xyz}(u_z, \psi, \theta, \phi)_z]^2} \quad (20)$$

where  $G_{xu}$ ,  $G_{yu}$ , and  $G_{zu}$  are the accelerations registered for the individual rotated sensor axis and the subscript  $z$  of the rotated vector is the vertical acceleration component. Incidentally, the resultant accelerations in the lateral and longitudinal directions are similarly obtained by multiplying the sensor values from the individual rotated accelerometers by the lateral and longitudinal components  $x$  and  $y$  respectively of the rotated unit vector.

## 4.4 Travel distance estimation

The maximum spatial resolution for the RIF is constrained theoretically by the maximum ratio of the accelerometer sample rate to the ground speed. Typical GPS receivers update much slower than accelerometers. Hence, the data processing algorithm interpolated between GPS updates to determine the distance traveled between accelerometer samples. Estimating the linear distance between GPS coordinate pairs and dividing by the number of accelerometer

samples provides a reasonably good estimate of the positions for peak RIF features of interest. For slower GPS updates, the product of the ground speed output, if available, and the system time will provide a fair estimate of the distance traveled since the last GPS update. It is not practical, however, to rely directly on the GPS receiver output to estimate travel distance because of large errors that occur from multipath reflections and occasional loss of satellite line-of-sight conditions. If the odometer reading is not available or the GPS receiver does not provide a ground speed output, then a Kalman filter is recommended to improve the estimated travel distance<sup>8</sup>. The approximate distance between a pair of GPS coordinates on the earth's surface where  $(\Theta_S, \Phi_S)$  and  $(\Theta_E, \Phi_E)$  denotes the start and end (latitude, longitude) pairs respectively is<sup>9</sup>

$$\Delta L = R_{earth} \left[ 2 \times \arcsin \left( \sqrt{\sin^2 \left( \frac{\Theta_S - \Theta_E}{2} \right) + \cos(\Theta_S) \times \cos(\Theta_E) \times \sin^2 \left( \frac{\Phi_S - \Phi_E}{2} \right)} \right) \right] \quad (21)$$

where  $R_{earth}$  is the mean earth radius of approximately 6371 kilometers.

## 5. RESULTS

The present IRI for any road segment is determined from the average RIF or TWIT presently computed, and a past RIF/IRI or TWIT/IRI ratio for that segment. The following sections compare the quality of data from the MnROAD and Bolley Drive traversals and use the RIF/IRI ratio obtained from the former to estimate the IRI.

### 5.1 Roughness characterization

The chi-squared statistic on the RIF data obtained for each road segment is tested on four distributions, namely the Gaussian, Student- $t$ , Log Normal, and Logistic<sup>10</sup>. Scale and translation parameters are introduced into each normalized distribution to best fit the data. The Gaussian model  $D_g(\xi)$  that estimates the distribution of the RIF variable  $\xi$  is

$$D_g(\xi) = \frac{\alpha_g}{\sqrt{2\pi\sigma_g^2}} \exp \left[ -\frac{1}{2} \left( \frac{\xi - \mu_g}{\sigma_g} \right)^2 \right] \quad (22)$$

where  $\alpha_g$ ,  $\mu_g$ , and  $\sigma_g$  are estimates of the amplitude, mean, and standard deviation parameters respectively. Similarly, the modified Student's  $t$ -distribution  $D_t(\xi)$  is

$$D_t(\xi) = \frac{\alpha_t}{\sigma_t} t_{df} \left[ \frac{\xi - \mu_t}{\sigma_t} \right] \quad (23)$$

where  $t_{df}(\xi)$  is the normalized Student's  $t$ -distribution, which is a gamma function of  $\xi$  and  $df$  degrees of freedom. The parameters  $\alpha_t$ ,  $\mu_t$ , and  $\sigma_t$  are estimates of the amplitude, mean, and standard deviation parameters respectively. The Log Normal distribution  $D_n(\xi)$  is

$$D_n(\xi) = \frac{\alpha_n}{\xi \sqrt{2\pi\sigma_n^2}} \exp \left[ -\frac{1}{2} \left( \frac{\ln(\xi) - \mu_n}{\sigma_n} \right)^2 \right] \quad (24)$$

The parameters  $\alpha_n$ ,  $\mu_n$ , and  $\sigma_n$  are estimates of the amplitude, mean, and standard deviation parameters respectively. The Logistic distribution  $D_L(\xi)$  is

$$D_L(\xi) = \frac{\alpha_L}{\sigma_L \left[ 1 + \exp \left( -\frac{\xi - \mu_L}{\sigma_L} \right) \right]^2} \exp \left[ -\frac{\xi - \mu_L}{\sigma_L} \right] \quad (25)$$

The parameters  $\alpha_L$ ,  $\mu_L$ , and  $\sigma_L$  are estimates of the amplitude, mean, and standard deviation parameters respectively.

Figure 6 compares the RIF distributions of the MnROAD traversals and the rough section of Bolley Drive. It is evident that even with significantly fewer MnROAD traversals, the variance is much smaller. Removing two outlier traversals that contained large GPS tagging errors provided the best possible data quality for comparing their fit with each of the four distributions. The higher consistency of the MnROAD data is due to a much smaller variance in traversal speed, more careful adherence to the wheel-path among traversals, and a doubling of the update rates for both the GPS and accelerometer sensors. The ground speed standard deviation for the rough segment of Bolley Drive was approximately

127 times higher than that of the MnROAD traversals. Nevertheless, from the Central Limit Theorem<sup>11</sup> the data consistency will improve with additional traversals. It is evident from these plots that each of the four distributions fit the data histogram in a similar manner. Figure 7 plots the RIF histogram and estimates of their distribution for relatively “smooth” and “rough” sections of Bolley Drive, and the rail grade crossing. The mean RIF for each segment is distinctly different as anticipated.

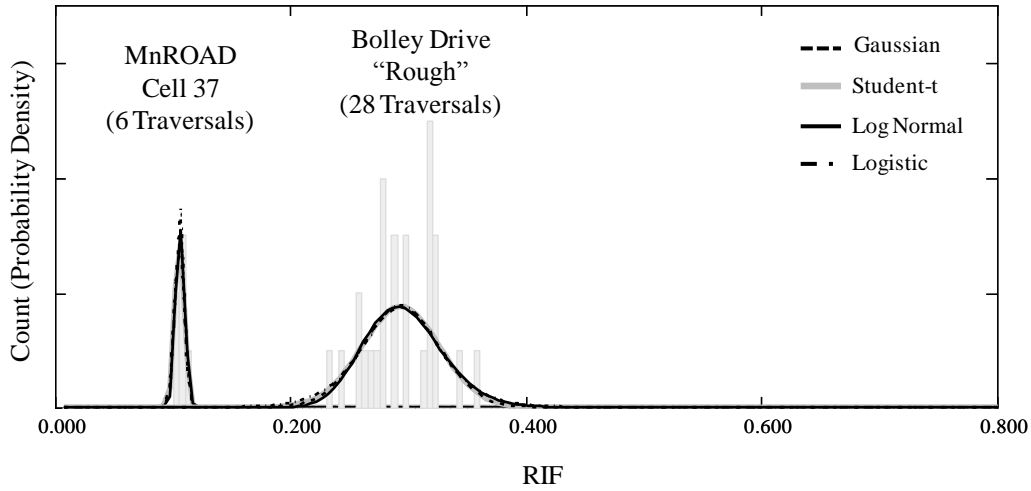


Figure 6. MnROAD IRI and RIF traversals.

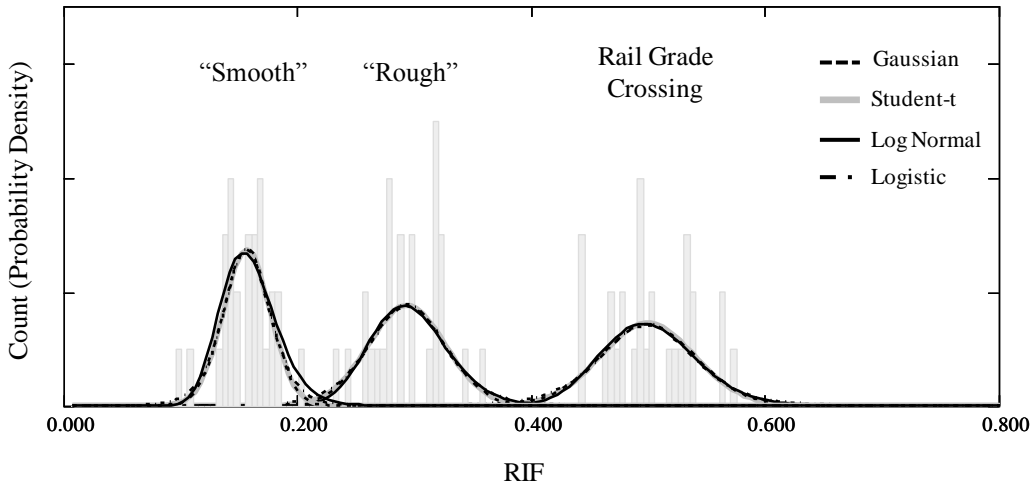


Figure 7. Bolley Drive traversals with the smartphone sensor.

Table 4 summarizes the parameter estimates for each of the four RIF distributions from the three Bolley Drive road segments and the MnROAD segment. The chi-squared value ( $\chi^2$  Data) listed in the table is calculated as

$$\chi^2 = \sum_{k=1}^n \frac{(O_k - E_k)^2}{E_k} \tag{26}$$

where  $O_k$  are histogram values observed in bin  $k$  and  $E_k$  are the expected values from the hypothesized distribution. The chi-squared distribution value for 5% significance ( $\alpha = 5\%$ ) is the largest value expected within 95% of the cumulative distribution. Hence, the significance percentage listed is the probability of observing a chi-squared value at least as large

as the value computed from equation (26). The chi-squared degrees of freedom,  $df$ , listed are determined as one less than the number of histogram data elements  $n$ , minus the two independent distribution parameters estimated, namely the amplitude and the standard-deviation, the latter being dependent on the estimate of the mean.

Table 4. Parameter estimates for the four RIF distributions on the four road segments.

	Smooth	Rough	Rail Grade	MnROAD
<b>Gaussian</b>				
$df$	157	157	157	48
$\chi^2 (\alpha = 5\%)$	187.239	187.239	187.239	65.171
$\chi^2$ Data	49.692	37.567	42.995	0.431
Amplitude	0.137	0.144	0.145	0.031
Mean	0.157	0.294	0.500	0.106
Standard Dev.	0.020	0.033	0.041	0.004
<b>Student-t</b>				
$df$	157	157	157	157
$\chi^2 (\alpha = 5\%)$	187.239	187.239	187.239	187.239
$\chi^2$ Data	46.713	37.409	43.423	0.442
Amplitude	0.137	0.145	0.145	0.031
Mean	0.157	0.294	0.500	0.106
Standard Dev.	0.020	0.033	0.040	0.004
<b>Log Normal</b>				
$df$	157	157	154	77
$\chi^2 (\alpha = 5\%)$	187.239	187.239	183.959	98.484
$\chi^2$ Data	57.006	38.628	43.006	0.259
Amplitude	0.157	0.144	0.145	0.031
LN(mean)	-1.847	-1.221	-0.693	-2.240
Standard Dev.	0.150	0.112	0.081	0.036
<b>Logistic</b>				
$df$	157	157	157	157
$\chi^2 (\alpha = 5\%)$	187.239	187.239	187.239	187.239
$\chi^2$ Data	24.643	38.497	44.993	0.680
Amplitude	0.144	0.150	0.149	0.032
Mean	0.157	0.294	0.499	0.106
Standard Dev.	0.013	0.021	0.026	0.002
Average RIF	0.155	0.294	0.502	0.108
MOE <sub>0.95</sub> (%)	5.659	3.993	2.807	3.516
V <sub>σ</sub> /V <sub>μ</sub> (%)	5.750	6.876	6.268	0.025

Statisticians generally reject a null hypothesis that the data follows a tested distribution if the significance level is less than 5%, or equivalently, if the computed chi-squared value ( $\chi^2$  Data) is greater than the chi-square distribution value at 5% significance. For these experiments, the computed chi-squared values are substantially smaller than the theoretical chi-squared value at 5% significance for all distributions tested. Consequently, a hypothesis that the RIF distribution follows any of the four distributions tested cannot be rejected. This result produces a high degree of confidence that the data fits classic distributions and that the variance of their mean will diminish with higher levels of vehicle traversals.

The margin-of-error (MOE) for a  $(1-\alpha)\%$  confidence interval with significance  $\alpha$  is

$$MOE_{1-\alpha} = \frac{S_{RIF} \times t_{1-\alpha/2,df}}{\sqrt{N_v}} \quad (27)$$

where  $N_v$  is the traversal volume and  $t_{1-\alpha/2,df}$  is the  $t$ -value where the cumulative  $t$ -distribution of  $df$  degrees of freedom is  $(1-\alpha)$ . The RIF standard deviation measured is denoted  $S_{RIF}$ . Table 4 lists the MOE<sub>0.95</sub> for the four road segments. As previously observed, the RIF variances for all of the Bolley Drive traversals are significantly larger than that of the MnROAD traversals, even for a much higher traversal volume. This result provides a high degree of confidence in the

quality of the MnROAD data, and hence the average RIF/IRI ratio measured of 0.069. As indicated in Equation (27) the MOE for all road segments will diminish with higher traversal volume.

**5.2 Roughness localization**

The RIF model provides a multi-resolution roughness characterization capability simply by changing the window length  $L$  of consecutive segments analyzed.

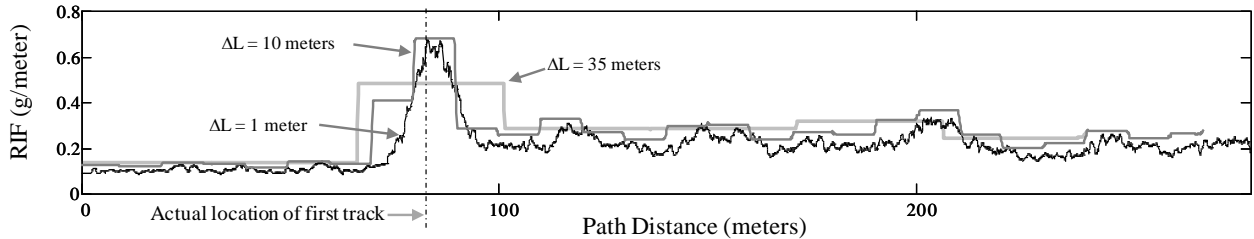


Figure 8. RIF of Bolley Drive at resolutions of 1, 10, and 35 meters.

To demonstrate this capability, the RIF for Bolley Drive is produced for window lengths of 1, 10, and 35 meters respectively. The RIF for each traversal is registered onto a higher resolution spatial grid and then ensemble averaged across the fixed windows. Figure 8 illustrates that the largest RIF values are distributed about the true location of the rail grade crossing. In this scenario, the peak RIF is located within one meters of the first track position with a standard deviation of 3.6 meters. Position errors arise from uncertainties that include variations in vehicle suspension transient responses and errors in GPS tagging. Hence, the resulting RIF distribution reflects the position uncertainty about the feature causing the roughness, and the position of the RIF peak as an estimate of the feature’s true position. The RIF levels from ensemble averaging may be color-coded for map-based visualization to identify the positions of peak roughness intensity. Future research will characterize and quantify the error components in feature position estimates.

**5.3 Vehicle characteristics and IRI estimate**

Figure 9 plots the sampled and estimated quarter-car frequency responses for the Inertial Profiler and the passenger vehicle.

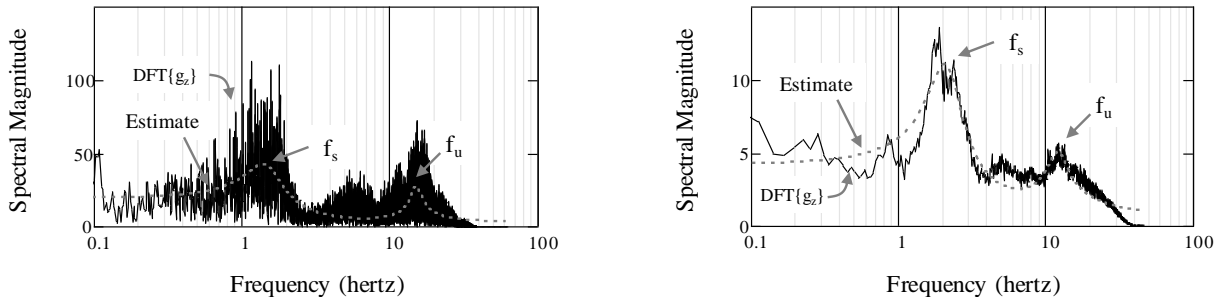


Figure 9. Frequency response estimates of the Inertial Profiler van (left) and instrumented passenger vehicle (right).

The passenger vehicle spectrum is an average of the 30 traversal spectra from the rough road segment.

Table 5. Parameter estimates for instrumented vehicles used in the case study.

Parameter	Units	Inertial Profiler Van		Passenger Vehicle	
		Sprung Mass	Unsprung Mass	Sprung Mass	Unsprung Mass
Resonant frequency ( $f$ )	Hz	1.5	15.18	2.19	12.56
Damping ratio ( $\zeta$ )	-	0.30	0.09	0.27	0.12
Response ratio ( $\rho_g$ )	-		4.3		2.4
Sensor calibration ( $\gamma_z$ )	-		0.79		0.89

The plots overlay the Discrete Fourier Transform (DFT) of the sampled vertical acceleration signal  $\{g_z\}$  vector and a

least squares fit of the quarter-car model. Table 5 summarizes the estimated model parameters. The frequency response of the Inertial Profiler van appears noisier than that of the passenger vehicle because the data came from a single traversal of a rough road segment that sufficiently excited the quarter car modes.

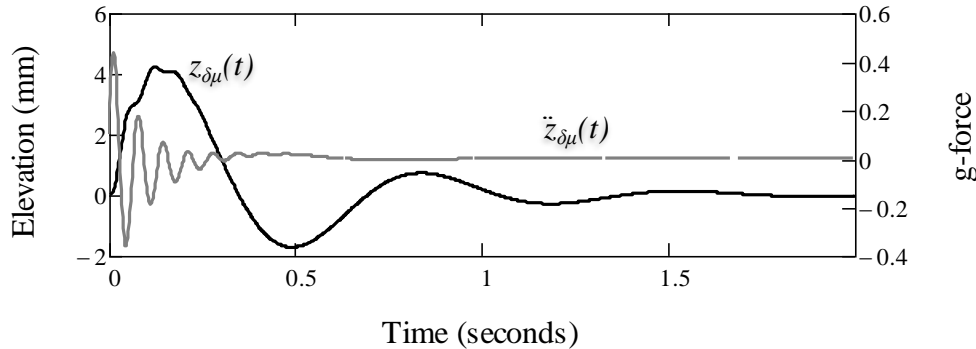


Figure 10. Impulse response and corresponding vertical acceleration of the passenger vehicle.

Unlike the data sampled from the passenger vehicle, additional inertial profiler traversals of the rough segment were not available for spectrum averaging.

Table 6. Parameter estimates for the four RIF distributions on the four road segments.

	Smooth	Rough	Rail Grade	MnROAD
IRI Estimate (m/km)	2.260	4.288	7.321	1.575
IRI Estimate (in/mile)	143.246	271.705	463.931	99.810
Qualitative	Mediocre	Poor	Poor	Fair

Figure 10 plots the quarter-car impulse response  $z_{\delta\mu}(t)$  and the corresponding vertical acceleration  $g_z(t) = \ddot{z}_{\delta\mu}(t)$  for the passenger vehicle suspension parameters estimated. Relative to the Golden Car impulse response shown in Figure 2, the passenger vehicle quarter-car impulse response contains a relatively smaller portion of the unsprung mass response. For this case study, the inertial profiler was not available to provide an IRI characterization for Bolley Drive. Therefore, the conversion factor estimated from the MnROAD characterization is used instead to produce the IRI estimates for Bolley Drive as summarized in Table 6. These values appear to correlate reasonably well to the relative differences in roughness observed.

## 6. SUMMARY AND CONCLUSIONS

A connected vehicle environment presents enormous opportunities to process voluminous GPS and inertial data to produce accurate and precise characterization of roughness, continuously. There is a lack of models to link statistics of mobility data to roughness indices that are equivalent to those currently used. This research derived a direct proportionality relationship between the RIF and the IRI from basic principles of the quarter-car impulse response. The direct proportionality is validated by producing both indices from an inertial profiler that traversed a test path at the MnROAD research facility. The careful control of speed and adherence to the wheel-path resulted in a much smaller RIF variance than that produced from a passenger vehicle traveling known rougher segments, even though the former involved only 6 traversals versus 28 for the latter. This experiment provided a high degree of confidence that RIF statistics follow classic distributions, including the Gaussian where the variance must diminish with higher traversal volume. Even with only 28 traversals of three distinctly different roughness segments, the 95% confidence interval about the mean was less than 6% for the smooth segment and only about 3% for the rail grade crossing. The corresponding IRI estimates were consistent with the relative roughness observed on the MnROAD traversals.

A connected vehicle environment is the ideal deployment scenario for the RIF model because precision improves with more data. Two additional features of the RIF is presented, namely a speed independent model called the TWIT, and a multi-resolution distress localization feature. The speed independent model produces a wavelength unbiased characterization of roughness. It is a linear combination of the RIF from vehicles traveling within different narrow speed bands, hence the TWIT is also directly proportional to the IRI. Pavement distress conditions that produce a sudden

vertical acceleration are detected simply by tagging locations where the RIF or TWIT levels exceed a pre-determined threshold. Those levels may be associated with a color for map-based data visualization and decision-support.

## ACKNOWLEDGEMENT

This work is based on research supported by the United States Department of Transportation (USDOT), Research and Innovative Technology Administration (RITA) under the Rural Transportation Research Initiative.

## 7. REFERENCES

- [1] Waite, A., Walsh, R., and Garcia, D., "Enabling a Secure Environment for Vehicle-to-Vehicle (V2V) and Vehicle-to-Infrastructure (V2I) Transactions," Proc. April 2012 Public Workshop FHWA-JPO-12-072, (2012).
- [2] Nagayama, T., Miyajima, A., Kimura, S., Shimada, Y., Fujino, Y., "Road condition evaluation using the vibration response of ordinary vehicles and synchronously recorded movies," Proc. SPIE 8692, (2013).
- [3] Dawkins, J., Bevely, D., Powell, B., and Bishop, R., "Investigation of Pavement Maintenance Applications of Intellidrive," University of Virginia Technical Report, (2011).
- [4] Gillespie, T. D., "Technical Considerations in the Worldwide Standardization of Road Roughness Measurement," University of Michigan Report to the World Bank, (1981).
- [5] Türkay, S., and Akçay, H., "Influence of tire damping on the ride performance potential of quarter-car active suspensions," IEEE Decis. Contr. P, (2008).
- [6] Bridgelall, R., "A Connected Vehicle approach for pavement condition monitoring," J. Infrastruct. Syst., (2013).
- [7] Gillespie, T. D., [CarSim Data Manual], Mechanical Simulation Corporation, Ann Arbor, (2004).
- [8] Brookner, E., [Tracking and Kalman Filtering Made Easy], John Wiley and Sons, (1998).
- [9] Gade, K., "A Non-singular Horizontal Position Representation," J. Navig., 63(3), 365-417, (2010).
- [10] Agresti, A. and Finlay, B., [Statistical Methods for the Social Sciences], Pearson, (2008).
- [11] Papoulis, A., [Probability, Random Variables, and Stochastic Processes], McGraw-Hill, New York, (1991).